## 5.1 Introduction

Vitamin C or ascorbic acid (AA), an organic compound, possesses antioxidant properties and is found in both plants and animals. It works as a redox buffer, lowers reactive oxygen species (ROS), and helps cancer prevention. The deficiency of AA in the human body may cause several issues like scurvy, drying of the mouth and eyes, dry irritated skin, hair loss, weariness, sleeplessness, tooth loosening, etc [Banavath et al., 2022; Pehlivan, F.E. 2017]. The regular intake range of AA in the body is 70-90 mg daily, which protects from scurvy. Previous studies suggest that a daily intake of more than 2000 mg (excess) per day may cause stomach cramps, diarrhea, and urinary stones [Levine et al., 1991; Rajpal et al., 2022]. In the optimum amount, it is used to improve the immune system, treat the common cold, heal mental sickness, and protect against cancer. So, monitoring AA in fruits and commercially available tablets and systematized intake is advisable for an efficacious medicinal approach. Thus, sensing AA has become crucial for a healthy body and has garnered international interest. Different techniques for sensing AA have been reported, including the electrochemical technique [Pisoschi et al., 2014; Atacan et al., 2022], Fluorescence [Liu et al., 2020], and colorimetric technique [Tarighat et al., 2022]. Due to its advantages of being affordable and simple to detect with the naked eye, the colorimetric approach has received a lot of interest [Tarighat et al., 2022; Ding et al., 2018; Sarkar et al., 2016; You et al., 2015].

Earlier, Natural enzymes were used in the colorimetric detection of many biomolecules and heavy metal ions. However, the expensive preparation and tedious purification process of natural enzymes limit their use [Wu et al., 2019; Liu et al., 2022]. In the last decade, nanozyme (non-natural enzymes) has been broadly used as a new variety of nanomaterial-based artificial enzymes [Wu et al., 2019]. Among them, metals and inorganic material-

based nanomaterials have profound applications exhibiting remarkable mimetic activity for the development of simple, low-cost, and naked-eye detection techniques with greater resistance to external environmental changes [Ojha et al., 2019; singh et al., 2021; Wang et al., 2021]. Although metal-based nanomaterials have proven themselves as remarkable mimic materials with wide applications such as peroxidases [Lyu et al., 2022], oxidases [Cao et al., 2017], haloperoxidases [Chen, Z. 2022], etc., they still suffer some limitations due to high cost, prone to aggregation, tedious synthetic routes, and storage complications [Zhu et al., 2022]. Carbon-based nanomaterial has become the most emerging and promising material in the field of nanoscience and technology [Verma et al., 2022; Chattopadhyay et al., 2022]. Among them, the two-dimensional (2D) carbon materials viz. Graphene [Cheng et al., 2022; Goswami et al., 2022] are extensively used in several applications, including sensing [Malik et al., 2022], energy storage [Xiao et al., 2022], and photocatalytic activity [Liu et al., 2021; Jaiswal et al., 2020]. The graphitic carbon nitride (g-$C_3N_4$) possesses structural similarities with graphene and has inherent nitrogen as part of its framework. It has a polymeric structure analogous to graphene. The tri-s-triazine (heptazine) acts as its repeating unit, and the material is characterized by high stability under acidic and basic environments.[Liu et al., 2021; Sharma et al., 2022],[Taha et al., 2021] g-$C_3N_4$ serves as a potential metal-free 2D material having the n-type semiconducting property that has gone under extensive research in the past two decades owing to its visible range absorption and non-toxicity. Inspired by the possible applications and the abundant demands for g-$C_3N_4$ nanocomposite, several methods have been established and explored in the last few years to explore its photo-based activities, such as photocatalytic dye degradation, water splitting, and fuel cells [Sharma et al., 2022; Taha et al., 2021; Ma et al.,

2019]. The g-$C_3N_4$ as nanosheets (NS) morphology exhibit enhanced features providing greater interaction of metal species via the

surface nitrogen. The nanosheet form of g-$C_3N_4$ has intrinsic peroxidase behavior that surface modification can further improve. For example, Fang Ma et al. have reported AuNPs functionalized g-$C_3N_4$ nanosheets showing good mimetic activity for α-fetoprotein, [Ma et al., 2019] Peng Ju et al. Prepared nanocomposite having $MoS_2$ quantum dots over $C_3N_4$ NS as an efficient artificial enzyme [Ju et al., 2018], F. Qiao et al. exhibited MnSe functionalized graphite phase carbon nitride nanosheets as enhanced peroxidase [Qiao et al., 2016]

It has been demonstrated that platinum nanoparticles (PtNPs) wrapped with a scaffold made of bovine serum albumin exhibit improved enzyme-mimicking activities, such as peroxidase, oxidase, and catalase-like activities [He et al., 2019]. In this work, we have immobilized Pt nanoparticles over g-$C_3N_4$ nano-sheets through a facile one-pot $NaBH_4$ reduction method. g-$C_3N_4$ was selected as a base material due to its biocompatibility. The synthesis of PtNPs decorated g-$C_3N_4$ nanocomposites (Pt@g-$C_3N_4$) was verified using Fourier-transform infrared spectroscopy (FT-IR) and X-ray diffraction techniques. The optical features were studied from UV-Vis absorbance spectra. Morphological analysis was performed using scanning and transmission electron microscopy (SEM and TEM). X-ray photoelectron spectroscopy (XPS) survey spectra confirmed the elements present in the nanocomposite. The as-prepared nanocomposite was then tested for a mimetic activity for oxidase mimic, and we found that it has an excellent affinity for 3,3',5,5'-tetramethylbenzidine (TMB), resulting in the formation of a blue charge transfer complex. The Pt@g-$C_3N_4$ nanocomposite sensor has been deployed for quantifying AA in buffer and real samples using its inhibition property. The developed sensor exhibits good linearity in

the concentration limit of 1-100 μM with a significant limit of detection 0.45 μM. This method was further tested for real samples (Orange, Lemon, and commercially available tablets), showing good recovery from 93-105%, and we have also developed a portable paper-based kit for detecting AA in real samples.

## 5.2 Experimental section

### 5.2.1 Materials

L-Ascorbic acid (assay ≥ 99%) was purchased from S D Fine-Chem Limited. 3,3',5,5'-Tetramethyl Benzidine (assay = 99.7%), Sodium acetate, Sodium chloride (NaCl), Calcium chloride ($CaCl_2$), Glacial acetic acid, Sodium hexachloroplatinate ($Na_2PtCl_6$), Acetate buffer, Glucose (Glu), Lactose (Lac), Galactose (Galac), Mannose (Man), Potassium chloride (KCl), Magnesium oxide (MgO), Citric acid (CA), Fructose (Fruc), and Sulphuric acid ($H_2SO_4$) were obtained from Sigma Aldrich. Orange, lemon, and Vitamin C tablets were purchased from grocery and medical shops. The ultrapure Milli-Q water (pH= 7 and resistivity=18.0 MΩ) was used in all experimental parts.

### 5.2.2 Synthesis of g-$C_3N_4$

g-$C_3N_4$ was prepared using urea as a precursor [Ong et al., 2016]. A certain amount of urea was stored in a covered alumina crucible and heated in a muffle furnace at 550°C at a ramping rate of 3°C/min for 4 hours. After completing the reaction, it was allowed to cool naturally, and a light-yellow fluffy material, i.e., g-$C_3N_4$ was recovered and preserved for further characterization.

### 5.2.3 Synthesis of Pt decorated g-$C_3N_4$

For the synthesis of Pt@g-$C_3N_4$, the first 10 mg of the synthesized g-$C_3N_4$ was uniformly distributed in 10 ml of double-distilled water through 6 hours of ultrasonication. After that, 1 mM of Pt salt ($Na_2PtCl_6$) was mixed into the water dispersion, preceded by the addition of 1% of $NaBH_4$ as a reducing agent under continuous stirring for half an hour. In the process, the yellowish color of the Pt@g-$C_3N_4$ reaction mixture was observed to change into bluish-grey upon reduction of Pt in the presence of $NaBH_4$. Thereafter, Pt@g-$C_3N_4$ nanocomposite was recovered by centrifugation at 8000 rpm followed by washing with the water-ethanol solution (1:1 in volume ratio). The resulting product was then vacuum dried at 80 °C for 2 h and stored for further experiments.

### 5.2.4 Instrumentations

The UV-Vis absorbance spectra were obtained from the Shimadzu UV-2600 spectrophotometer, while an EPOCH microplate reader (Biotek) was used for examining the enzyme mimic activity of Pt@g-$C_3N_4$. The NICOLET iS5 equipment from Thermo Scientific was used to capture the FT-IR spectra. The diffraction patterns were recorded from Rigaku Miniflex 600 X-ray diffractometer, and the images of the nanocomposite were obtained from FEI's TECHNAI G2 20 TWIN and FEI NOVA NANO SEM 450 instruments. XPS spectra were recorded from K-alpha model of Thermo Fischer Scientific XPS instrument. The image was captured by a smartphone with a camera (64-megapixel), Android 12, and Funtouch OS 12 Global operating system (Vivo Y73).

### 5.2.5 Choice and Preparation of Material

With outstanding catalytic performance, high surface area, high functionalization, small size, high stability, biocompatibility, and cost-effective preparation, g-$C_3N_4$ has potential application in photocatalytic and energy storage devices [Ngo et al., 2020; Zhang et al., 2020]. For the detection of ascorbic acid using a colorimetric technique, there is a need to develop an enzyme mimic. Oxidase mimic was chosen as it protects us from the use of corrosive $H_2O_2$ in the case of peroxidase-based techniques. The oxidase property of g-$C_3N_4$ is poor, and therefore there is a need to improve its oxidase catalytic properties, which was achieved by modifying it with PtNPs. Pt@g-$C_3N_4$ exhibited excellent oxidase mimetic behavior, as shown in Figure 5.3 (a).

### 5.2.6 Study of oxidase activity of Pt@g-$C_3N_4$ nanozyme

To study the oxidase properties of Pt@g-$C_3N_4$, absorption spectra were recorded in various combinations. The designated combinations include: (a) 1+2+3 (b) 1+2+4 (c) 1+2 (d) 1+2+3+5 where, '1' is TMB (50 μL; 200 μM), '2' is 200 μl 0.1 M Acetate buffer (pH 4), '3' is 15μl 1 mg/ml Pt@g-$C_3N_4$, '4' is 15 μl of 1 mg/ml g-$C_3N_4$, and '5' is 30 μL of 1 M $H_2SO_4$.

### 5.2.7 Colorimetric assay of AA

The oxidase property of the developed nanozyme is used to quantify AA using the colorimetric probe. In experimentation, 200 μl 0.1 M acetate buffer (pH 4), 100 μL AA (1 to 100 μM), and 15 μL of Pt@g-$C_3N_4$ (0.05 mg/L) were taken together into a 500 μL Eppendorf. Thereafter, the 50 μL of TMB was spiked into the mixture solution. The 300 μL of the final mixture solution was pipette-in into a 96-well ELISA plate after incubating for

half an hour, and the stop solution ($H_2SO_4$) was added to the above mixture solution. The UV absorption endpoint was recorded at 450 nm of wavelength characteristics to completely oxidize TMB.

## 5.3 Results and Discussion

### 5.3.1 Characterization of Nanozyme

The large surface-to-volume ratio of the 2-D material is crucial for bio-sensing applications. Figure 5.1 (a) depicts the UV-Vis absorption plot of g-$C_3N_4$ and Pt@g-$C_3N_4$. The absorbance edge of g-$C_3N_4$ is found around 420 nm, typical of g-$C_3N_4$. However, a bathochromic shift is observed in the absorption peak of Pt@g-$C_3N_4$, indicating that an interaction between Pt nanoparticles with the g-$C_3N_4$ causes higher stacking of nanosheets. To get insight into the change in the optical gap ($E_g$) owing to Pt incorporation into g-$C_3N_4$, the well-known Tauc relation [Jana et al., 2022] has been utilized,

$$\alpha h\nu = C\left(h\nu - E_g\right)^m \quad \text{..... (Eq. 5.1)}$$

where $\alpha$, $h$, $\nu$, $m, C$, and $E_g$ represent absorption coefficient, Planck's constant, optical frequency, order-of-transition ($m = {}^1/_2$; considering the electronic transition for both the samples a direct-allowed type), a proportionality constant, and optical gap, respectively. The optical bandgap has been estimated from the $(\alpha h\nu)^2$ $vs$ $h\nu$ plot as shown in Figure 5.1 (a), and it was found to be decreased in Pt@g-$C_3N_4$. Thus, it can be argued that Pt incorporation increased the overall electron density in g-$C_3N_4$ and caused the reduction in the optical gap, which will momentarily enhance the oxidase activity of the nanozyme towards AA sensing.

Next, to study the crystallinity of g-$C_3N_4$ and Pt@g-$C_3N_4$ nanomaterials, XRD is used. Figure 5.1 (b) reveals that an intense diffraction peak located at 27° in $C_3N_4$ corresponds to

the (002) plane (JCPDS Number: [01–087-1526]), which confirms its graphite-like structure with an interlayer spacing of 3.234 Å. While in Pt@g-$C_3N_4$, four other diffraction peaks located around 39.5°, 45.68°, 67.95°, and 81.44° appeared along with the primary peak of g-$C_3N_4$. The four diffraction peaks of these Pt nanoparticles, which correspond to the face-centered cubic phase, were designated as (111), (200), (220), and (311) [Fahmy et al., 2020]. The Scherrer relation has been used to evaluate the average crystallite size for both g-$C_3N_4$ and Pt@g-$C_3N_4$ [Hanif et al., 2022],

$$L_c = \frac{K\lambda}{\beta Cos\theta}$$

Where β represents integrated peak-width at half maxima, K represents the shape factor (= 0.94), and λ (the radiation wavelength) = 1.541862Å. Thus, the incorporation of Pt nanoparticles in g-$C_3N_4$ was found to enlarge the average crystallite size from 7.6 nm to 8.2 nm, which also supports the reduction of the bandgap by increasing the effective bandwidth. Different functional groups present in both samples have been probed through FT-IR, where peaks from 3300 to 3000 $cm^{-1}$ show the vibration mode for N-H stretching, as shown in Figure 5.1 (c). The peak corresponding to 807 and 889 $cm^{-1}$ is the characteristic peak of hexagonal tri-s-triazine and N-H bending mode, respectively [Ojha et al., 2022]. The distinctive stretching modes of the C-N heterocycle are attributed by vibrational peaks in the region of 1641–1236 $cm^{-1}$.

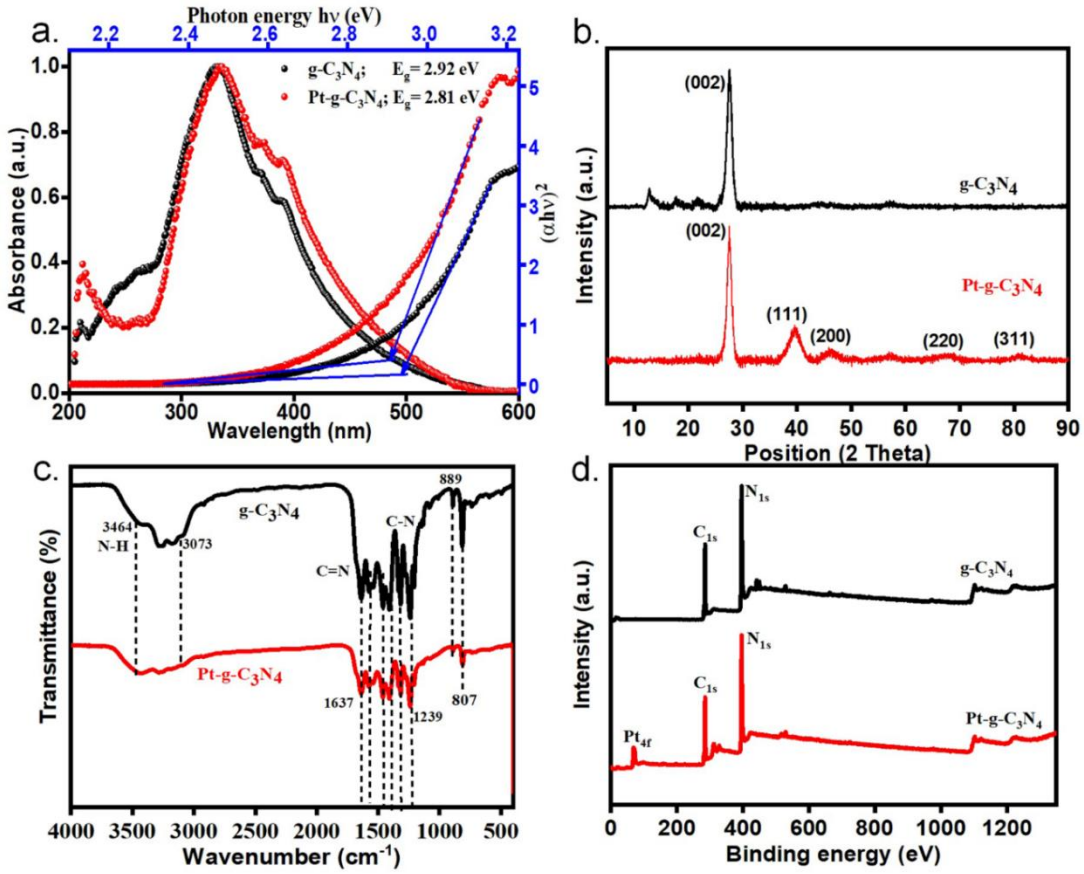


**Figure 5.1** (a) UV-visible spectra and corresponding Tauc plot, (b) XRD pattern (c) FT-IR spectra and (d) XPS survey spectra of g-$C_3N_4$ and Pt@g-$C_3N_4$.

From the FT-IR peaks, it is clear that even after the Pt nanoparticle growth over the g-$C_3N_4$ surface, the chemical structure of g-$C_3N_4$ persists completely except for minor vibrational changes. The intensity ratio difference between Pt@g-$C_3N_4$ and g-$C_3N_4$ i.e. 889/807, proves that Pt and N interact through some secondary bond formation [Rezaei et al., 2018]. XPS survey spectra also show that Pt is present in the surroundings of g-$C_3N_4$, as shown in Figure 5.1 (d). The sheet-like morphology of both samples is confirmed from SEM characterization (Figure 5.2 a&b). While TEM images show that Pt nanoparticles distributed randomly over the exfoliated g-$C_3N_4$ nanosheets, as shown in Figure 5.2 (d).

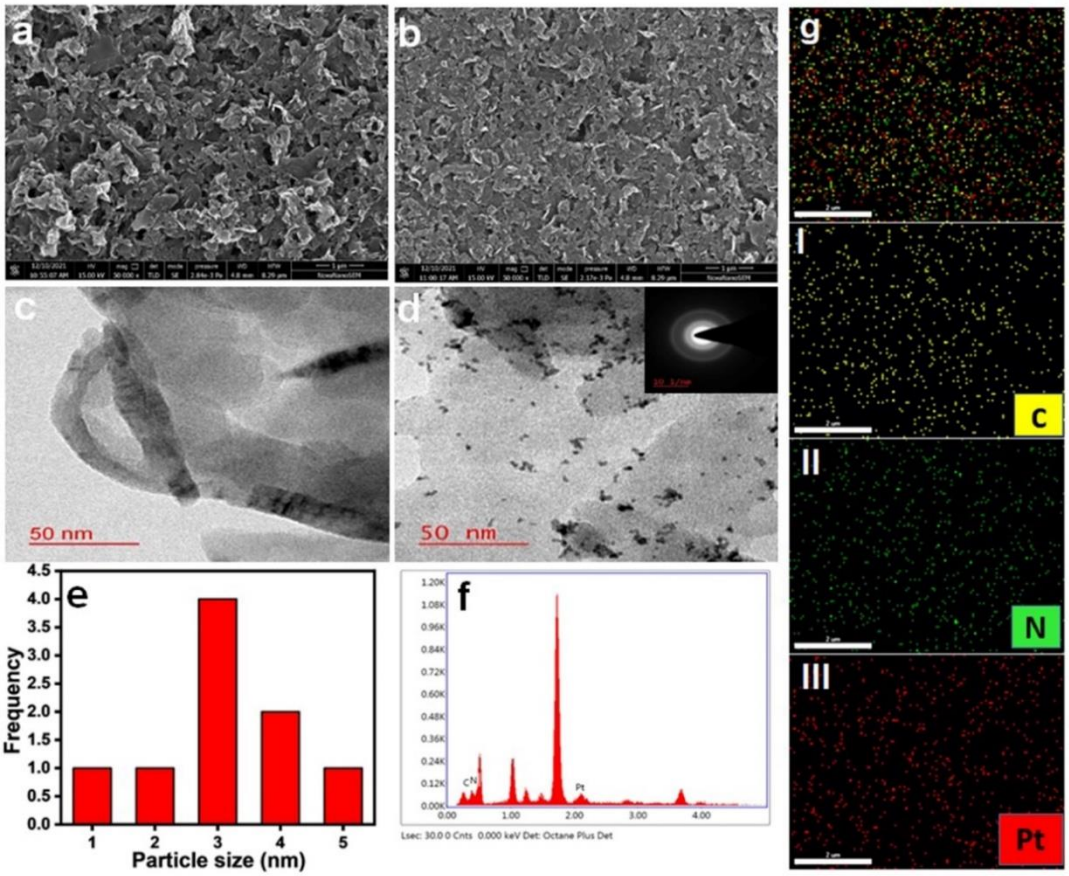


**Figure 5.2** Scanning electron microscopy images of (a) g-$C_3N_4$ and (b) Pt@g-$C_3N_4$; TEM image of (c) g-$C_3N_4$ and (d) Pt@g-$C_3N_4$; inset shows corresponding SAED pattern; (e) Particle-size distribution curve of Pt nanoparticles anchored over the g-$C_3N_4$; (f) EDX spectrum of the Pt@g-$C_3N_4$ and (g) elemental mapping of Pt@g-$C_3N_4$ corresponding to (i) C, (ii) N, (iii) Pt respectively.

The particle size distribution histogram confirms that the majority of the particles are 3 nm in size, with a size range of 1 to 5 nm (Figure 5.2 (e)). Elements carbon, nitrogen, and platinum are all represented by elemental mapping in Figure 5.2 (g) (i, ii, and iii), which reveals that these elements are present over the nanosheets in a well-distributed manner. The EDX analysis in Figure 5.2 (f) shows the relative amount of all elements present in the Pt@g-$C_3N_4$ and reveals that the platinum concentration is very low compared to C and N elements. The extra peak besides Pt is due to the presence of precursor moiety present in

synthesized material, oxygen ($SiO_2$), and silica glass used for the drop cast of material. The major peak besides Pt is due to Si from the glass substrate and minor peaks are coming due to the adsorbed oxygen. It verifies our strategy to use a minimum optimum amount of costly metal salt to get the best cost-to-performance ratio for the sensor.

### 5.3.2 Oxidase-like activity of Pt@g-$C_3N_4$

The oxidase property of synthesized nanocomposite, Pt@g-$C_3N_4$ was investigated using a chromogenic substrate. TMB alone had rarely shown any color change and oxidation without Pt@g-$C_3N_4$, as shown in Figure 5.3 (a) curve c. The formation of a blue-colored charge transfer product with an absorbance peak at 652 nm is the result of the Pt@g-$C_3N_4$ catalyzing the oxidation of TMB in the presence of dissolved oxygen, as illustrated in Figure 5.3 (a) curve a (black line).

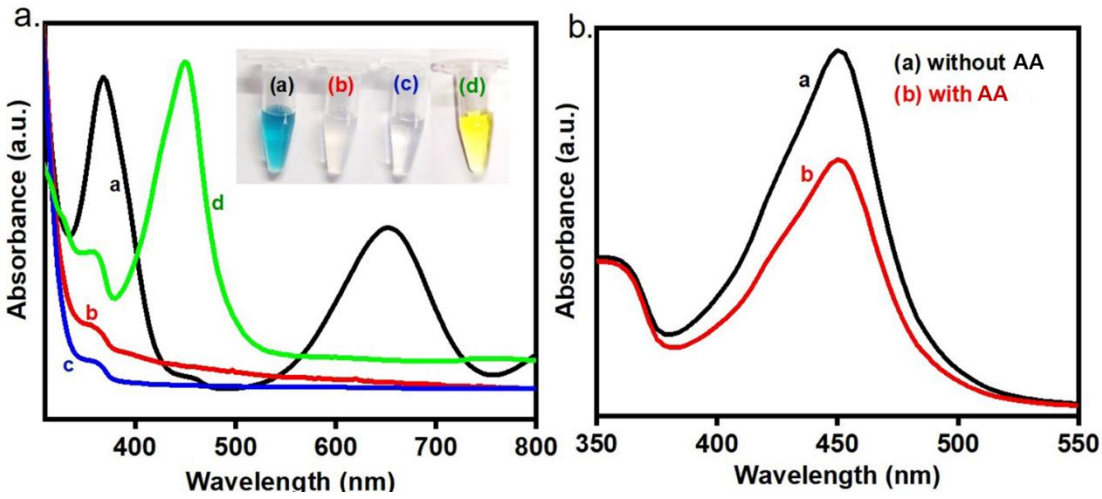


**Figure 5.3** (a) UV-visible spectrum for different combinations (a) 1+2+3 (b) 1+2+4 (c) 1+2 (d) 1+2+3+5 where, '1' is TMB, '2' is Acetate buffer, '3' is Pt@g-$C_3N_4$, '4' is g-$C_3N_4$, and '5' is $H_2SO_4$. (corresponding color contrast shown in inset) (b) the absorbance spectra (corresponding to 450 nm) in the presence and absence of AA at pH 4.

In a subsequent step, stop solution $H_2SO_4$ was added, which resulted in the formation of a yellow color diimine complex exhibiting the absorbance maxima at 450 nm (Figure 5.3 (a) curve d) [Verma et al., 2022]. In control, we have also investigated the oxidase properties of g-$C_3N_4$, as shown in Figure 5.3 (a) curve b. g-$C_3N_4$ alone does not cause TMB oxidation, supporting the hypothesis that the oxidase-like activity arises as a result of the nanocomposite formation. Figure 5.3 (b) depicts the absorbance spectra (corresponding to 450 nm) in the presence and absence of AA. The absorbance intensity gets diminished in the presence of AA due to its free radical scavenging nature [Zhang et al., 2022].

### 5.3.3 Dependence of the oxidase activity of Pt@g-$C_3N_4$ on the pH and temperature

Various parameters like pH and temperature play important roles in Pt@g-$C_3N_4$ mimic activity. To optimize the pH of the solution mixture, buffer solutions of different pHs viz. 2, 3, 4, 5, 6, 7 and 8 were prepared using acetate buffer, phosphate buffer, and carbonate buffer. Figure 5.4 (a) represents the endpoint absorption spectra at 652 nm corresponding to different pH solutions. It can be observed that nanozyme

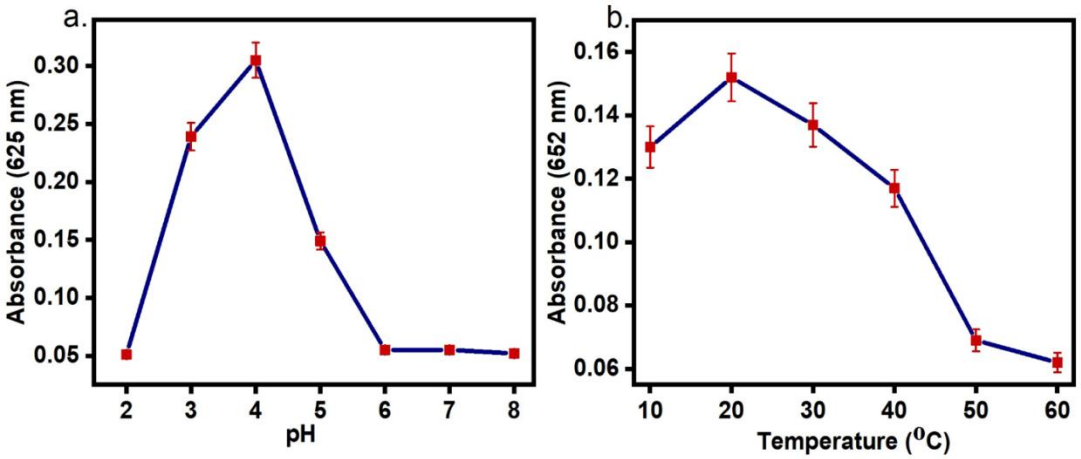


**Figure 5.4** Endpoint absorption spectra (a) Optimization of pH and (b) Temperature.

exhibited maximum catalytic activity at pH 4, which is in accordance with previous reports.[Lin et al., 2014] We used the ice water and hot plate to optimize the temperature at 10, 20, 30, 40, 50 and 60 $^{o}$C. The endpoint absorption spectrum versus temperature graph, as shown in Figure 5.4 (b) for oxidase activity of Pt@g-$C_3N_4$ reveals that it has temperature-dependent mimetic activity with maximum activity observed at 20$^{o}$C, this is in contrast to natural enzymes.

### 5.3.4 Kinetics assessment of Pt@g-$C_3N_4$

The oxidase-like activity of Pt@g-$C_3N_4$ was studied by steady-state kinetic experiments. The data for the kinetic study were obtained by varying the TMB concentration from 10 to 400 μM and keeping a fixed concentration of Pt@g-$C_3N_4$ (0.05 mg/ml), as shown in Figure 5.5 (a). As can be inferred at the initial stage (at lower TMB concentration i.e., below 200μM), there is a linear response between the nanozyme velocity and TMB concentration, but when concentration becomes higher, enzyme velocity becomes independent of TMB concentration. This is the saturation region for the catalyst. The oxidase-like activity of Pt@g-$C_3N_4$ follows Michaelis Menten's behavior in a particular concentration range of TMB (10 to 400 μM). The maximum velocity indicated as $V_{max}$ and Michaelis-Menten constant indicated as $K_m$ were calculated by linear fitting of Lineweaver plot using mathematical statement 1.

$$v = \frac{V_{max}[S]}{K_m + [S]} \qquad \text{.....(Eq. 5.2)}$$

Here, v represents the velocity of the reaction, while S is substrate concentration. From the Lineweaver-Burk plot, we are getting $V_{max}$ value at 9.69 × $10^{-6}$ $S^{-1}$M and $K_m$ value at 55.3

μM (Figure 5.5 (b)). The lower $K_m$ value of Pt@g-$C_3N_4$ to the natural enzyme horseradish peroxidase (HRP: 434 μM) signifies greater affinity of Pt@g-$C_3N_4$ for TMB, while the higher value of $V_{max}$ in comparison to HRP ($14.72 \times 10^{-8}$ $s^{-1}$) represents the better catalytic activity of Pt@g-$C_3N_4$ [Chen et al., 2014],[Wu et al., 2019].

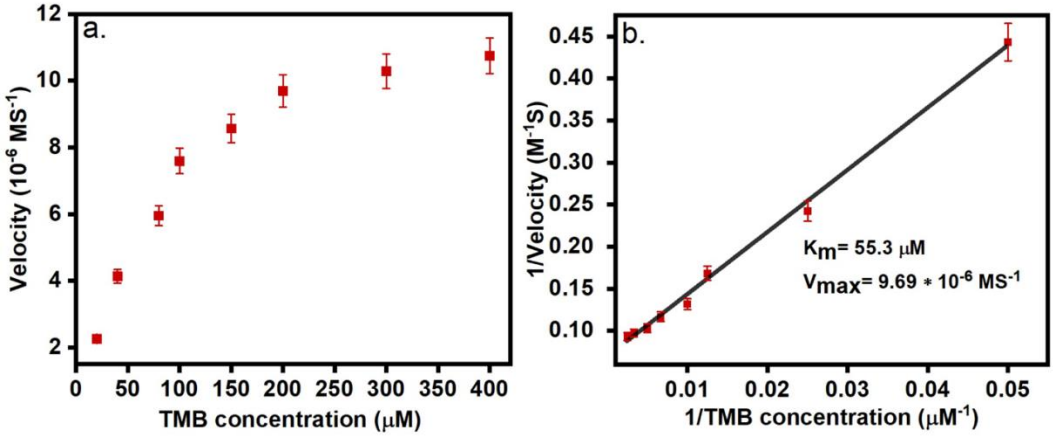


**Figure 5.5** (a) Optimization of TMB (b) Lineweaver-Burk plot in the presence of acetate buffer, TMB, and Pt@g-$C_3N_4$

**Table 5.1** Comparison of $K_m$ and $V_{max}$ of TMB with Pt-$C_3N_4$ and different nanomaterials.

| **Catalytic substrate** | **$K_m$ (μM)** | **$V_{max}$ ($S^{-1}M$)** | **Reference** |
|---|---|---|---|
| **Pt-g-$C_3N_4$** | 55.3 | $9.69 \times 10^{-6}$ | This work |
| **AuNPs** | 110.0 | $15.39 \times 10^{-9}$ | [Xue et al., 2021] |
| **AuNPs@$C_3N_4$** | 97.0 | $1.52\times 10^{-8}$ | [Wu et al., 2019] |
| **HRP** | 434.0 | $10 \times 10^{-8}$ | [Chen et al., 2014] |

A comparison table as Table 5.1 in supporting information provides the Km value and enzyme velocity of Pt@g-$C_3N_4$ and other reported nanozymes. The table shows a better response of our nanocomposite Pt@g-$C_3N_4$ for oxidase activity compared to HRP and other previous reports.

Figure 5.6 gives a plausible explanation for how Pt@g-$C_3N_4$ works as a catalyst. Using EPR and optical spectroscopy, it has been well established that TMB oxidation occurs in the presence of a catalyst.[Ojha et al., 2021] In favor of this, the oxidation of TMB molecules to diimine has been described in Figure 5.6 TMB absorbs electromagnetic radiation in its reduced form at $\lambda_{max}$=285 nm and shows no colour. Although a blue color product is obtained in the presence of dissolved oxygen and an active oxidase catalyst. During the oxidation process of TMB as depicted in Figure 5.6 (i), a cation-free radical is formed, transforming into a blue color charge transfer complex (CTC) equilibrating with the unoxidized form of TMB, showing absorption maxima at 370 and 652 nm.

Furthermore, when $H_2SO_4$, i.e., stop solution, is added, the pH drops from 4 to roughly 1, and the equilibrium shifts to radical cations to form a diimine product (yellow product) having $\lambda_{max}$ of 450 nm (Figure 5.6 (ii)) and a greater molar absorptivity [Verma et al., 2022]. Since AA acts as a competitive inhibitor of TMB molecules and inhibits their oxidation. Therefore, color contrast is developed with different concentrations of the AA.

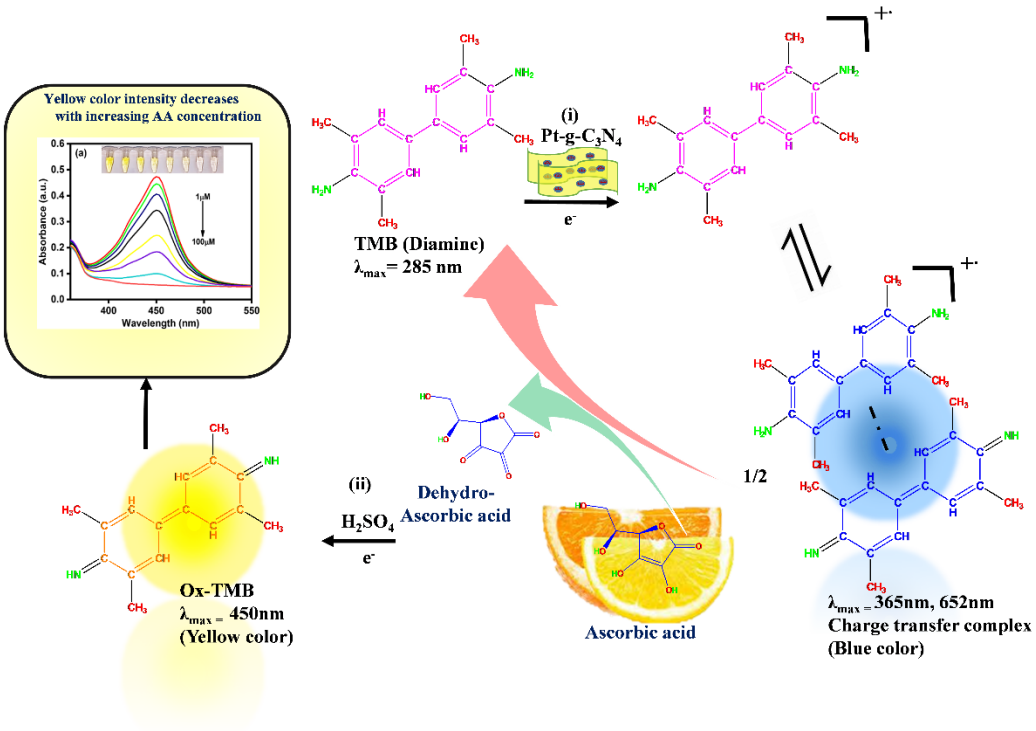


**Figure 5.6** Schematic demonstration of TMB's oxidation using Pt@g-$C_3N_4$.

### 5.3.5 Sensing of Ascorbic acid using Pt@g-$C_3N_4$

Under the optimized conditions, the developed methods were tested for the detection of AA. Since AA has an inhibitory effect on Pt@g-$C_3N_4$ oxidase activity and is concentration-dependent, this inhibitory effect is also confirmed by cyclic voltammetry (Figure 5.6) measurement. Cyclic voltammetry is an essential tool for knowing the catalytic behavior of a catalyst. Under the optimized condition, the effect of pH on the catalytic activity was acquired by using an acetate buffer. We are using a standard three-electrode system with a Pt-g-$C_3N_4$ modified glassy carbon electrode-based working electrode, Ag/AgCl as a reference, and Pt electrode as a counter electrode for the electrochemical measurements. Before performing the experiments, high-purity $N_2$ gas was purged for 5 minutes into the electrolyte solution, working electrodes were dipped into the electrolyte for 10 minutes each

for better electrolyte diffusion, and then 20 CV cycles were run for proper stabilization of the system (at a constant temperature). Figure 5.7 shows a double peak for oxidation potential (0.4 and 0.65 V vs Ag/AgCl) of TMB in acetate buffer in the CV curve. These two peaks are related to the oxidation by losing one or two electrons to form a blue or yellow product with a peak of 652 nm or 450 nm, respectively [Liu et al., 2019; Zhan et al., 2022] The CV curve corresponding to g-$C_3N_4$ has a low current implying poor mimetic activity. So, the synergistic effect in the catalytic activity of nanocomposite is important for mimetic behavior, which is clearly seen in the case of Pt-decorated g-$C_3N_4$. While the current ranges in TMB(ox) substrate oxidations were 4.32 μA and 3.77 μA, respectively, with the addition of AA, the current values dropped to 2.78 μA and 2.98 μA, respectively, showing the quenching effect.

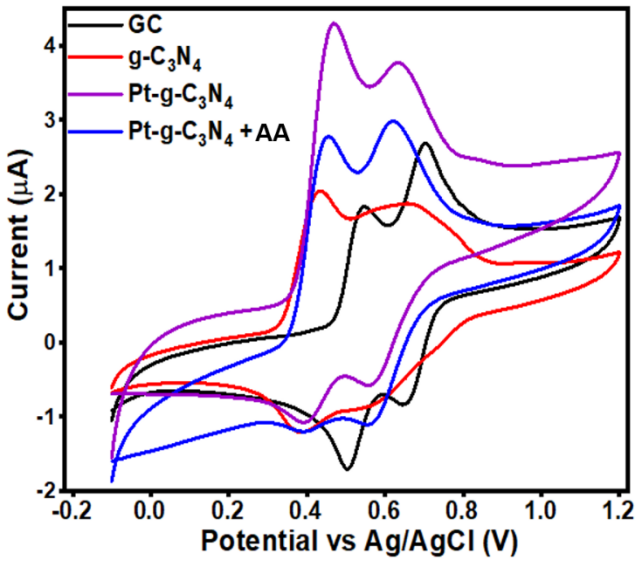


**Figure 5.7** Cyclic voltammetry study carried out in aqueous medium i.e. TMB in acetate buffer solution (pH = 4, concentration = 1 mM, scan rate = 20 mV/s, working electrode = glassy carbon electrode; geometrical area: 0.07 $cm^2$)

TMB undergoes an oxidation reaction mediated by Pt@g-$C_3N_4$, which results in the formation of a blue-colored product. When the stop solution is added, the blue color changes to yellow, resulting in a 450 nm absorbance peak. The addition of different concentrations of AA gives a color contrast. Figure 5.8 (a) depicts AA's sensing, demonstrating that the produced sensor has excellent linearity in the region of 1 to 75 μM and a regression coefficient of 0.99 [Linear regression equation: Y = mX + c, Y (wherein m= -0.00503 ± 0.00016, and c= 0.44 ± 0.01 from the calibration plot) is the dependent variable, m is the slope, X is the independent variable, and c is the intercept]. The linear calibration plot, shown in Figure 5.8 (b), was produced using the average of ten replicates. A limit of detection of 0.45 μM was computed using the formula Limit of detection (LOD) = 3*σ/m (wherein σ is the blank standard deviation and m is the slope of the calibration curve).

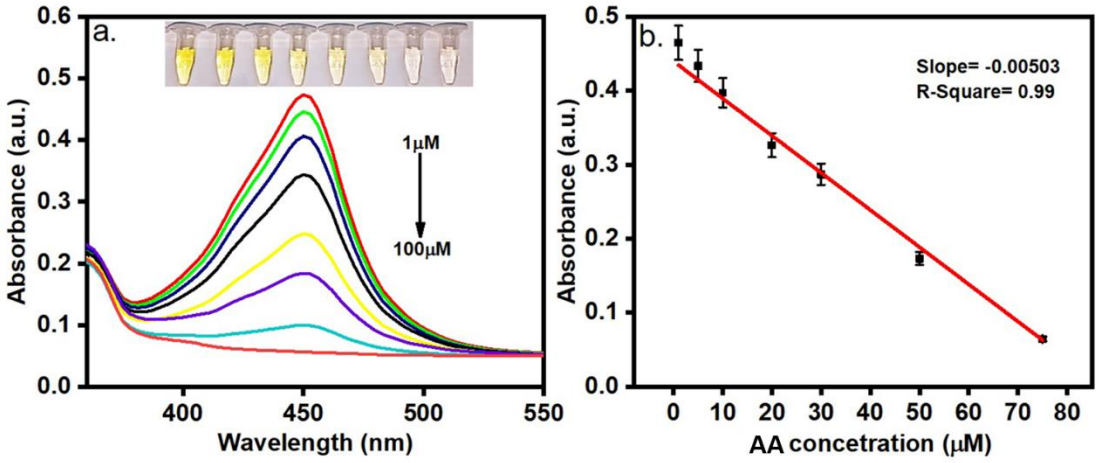


**Figure 5.8** (a) The UV-visible absorption spectrum for different concentrations of AA (1, 5, 10, 20, 30, 50, 75, 100 μM) in aqueous medium at pH 4 (b) Linear calibration plot. (In the inset of the Figure (a), the image of color developed corresponds to the AA concentration is shown.)

The comparison table for LOD and linear range of AA for Pt@g-$C_3N_4$ and different nanomaterials have been compared in table 5.2. From this, it is exemplified that our material can successfully sense the AA with good linearity and better detection limit.

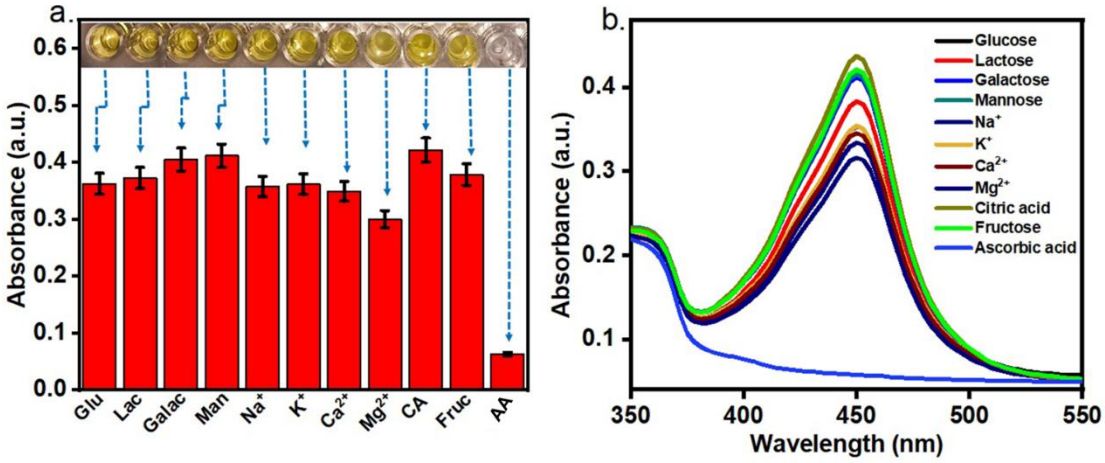


**Figure 5.9** (a) Selectivity of AA in the presence of different interfering agents (Glu, Lac, Galac, Man, $Na^+$, $K^+$, $Ca^{2+}$, $Mg^{2+}$, CA, Fruc, AA) and (b) Corresponding spectral diagram.

### 5.3.6 Interference study of AA detection

The selectivity of sensors is used as an essential parameter to confirm its reliability for the test of real samples. We opted for different possible biomolecules and ions for the interference study of AA. We have taken ten times the concentration of interfering agents (like Glu, Lac, Man, Na, K, Ca, Mg, CA, Fruc and galac) in comparison to AA (concentration 100 μM). The result, as shown in Figure 5.9 (a), suggests that even at ten times the concentration of the interfering agent, the inhibition property of AA is far more pronounced, justifying the selectivity of the developed sensing strategy. Figure 5.9 (b) shows the spectra corresponding to the different interfering agents given above.

**Table 5.2** Comparison table for LOD and linear range of Ascorbic acid for Pt-$C_3N_4$ and different nanomaterials

| **Material** | **Method** | **LOD (μM)** | **Linear range (μM)** | **References** |
|---|---|---|---|---|
| **Cu/Ag/rGO** | Colorimetry | 3.6 | 1-30 | [Darabdhara et al., 2017] |
| **AgFKZSi$W_{12}$/PPy** | Colorimetry | 2.7 | 1-80 | [Li et al., 2019] |
| **MIL-68/MIL-100** | Colorimetry | 6 | 30-485 | [Zhang et al., 2014] |
| **FeMnzyme** | Colorimetry | 0.88 | 8-56 | [Han et al., 2022] |
| **CuFKZ$P_2W_{18}$/PPy(15%)** | Colorimetry | 0.627 | 5-100 | [Li et al., 2020] |
| **$CuCo_2O_4$ Microspheres** | Colorimetry | 0.57 | 1-10 | [Han et al., 2021] |
| **Pt-$C_3N_4$** | Colorimetry | 0.45 | 1-140 | This work |

### 5.3.7 Durability and recyclability study

Stability and recyclability are important aspects of catalysts, especially with expensive metals. The reusability of the Pt@g-$C_3N_4$ nanozyme is examined and shows that the catalytic activity can be maintained at room temperature. The recyclability and repeatability were tested several times using **.**the freshly prepared solution, as shown in Figure 5.10 (a) & (b). In order to perform the recyclability test, post nanozyme application, it was recovered by centrifugation at 6000 rpm for 15 min. Further, it was tested for its oxidase property. As shown in Figure 5.10 (a), Pt@g-$C_3N_4$ exhibited almost similar activity over five cycles (~95%). The little reduction is due to the loss of material during centrifugation. From Figure 5.10 (b), the sensor's relative activity can be seen to be similar for up to 10 days without significantly changing.

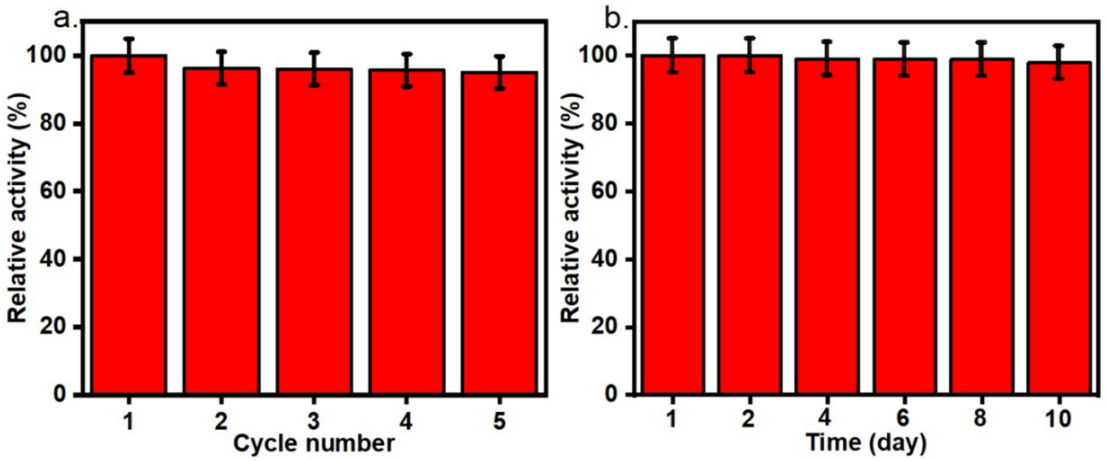


**Figure 5.10** (a) Cycle stability and (b) Reproducibility study over different days.

### 5.3.8 Recovery study

Citrus fruits like oranges and lemons are a vital source of ascorbic acid or vitamin C, having antioxidant properties towards reactive free radicals and non-radicals generated during metabolic reactions in the human body. Hence the assessment of AA content by the developed sensor in real samples is essential from a real perspective.

**Table 5.3** Analytical recovery study results of AA in real samples.

| 50 Fold diluted | Spiked AA (μM) | Found AA (μM) | Recovery |
|---|---|---|---|
| **Orange** | **0** | **39.57** | **100%** |
| | **10** | **51.32** | **100.6%** |
| | **20** | **58.13** | **97.6%** |
| **Lemon** | **0** | **45.58** | **100%** |
| | **10** | **55.96** | **100.7%** |
| | **20** | **66.17** | **100.89%** |
| **Tablet (20 μM)** | **0** | **18.54** | **92.7%** |
| **30 μM** | **10** | **31.72** | **105.7%** |
| **40 μM** | **20** | **40.09** | **100.2%** |

We have monitored AA activity in fruit samples and commercially available tablets. So, we have added various known concentrations of AA (10, 20 μM) to the 50-fold diluted lemon, orange and 20 μM tablet samples and identified by the proposed sensing probe. From the perusal of table 5.3, it can be observed that the mean recoveries for the Lemon, Orange, and tablet samples ranged between 92.7% and 105.7%, which is suitable for the quantifiable analysis of AA in samples. As shown in Table 5.3, the experimental results demonstrate the

reliability and accuracy of the colorimetric sensor platform for AA detection in real samples.

### 5.3.9 Portable Kit

The developed sensor is considered useful, if it is easy to use for onsite samples. To achieve this goal, we proposed a paper-based portable kit for real-time detection of AA (Figure 5.11). The portable kit was assembled using simple Whatman paper shaped into 1×3 $cm^2$ rectangular sizes.

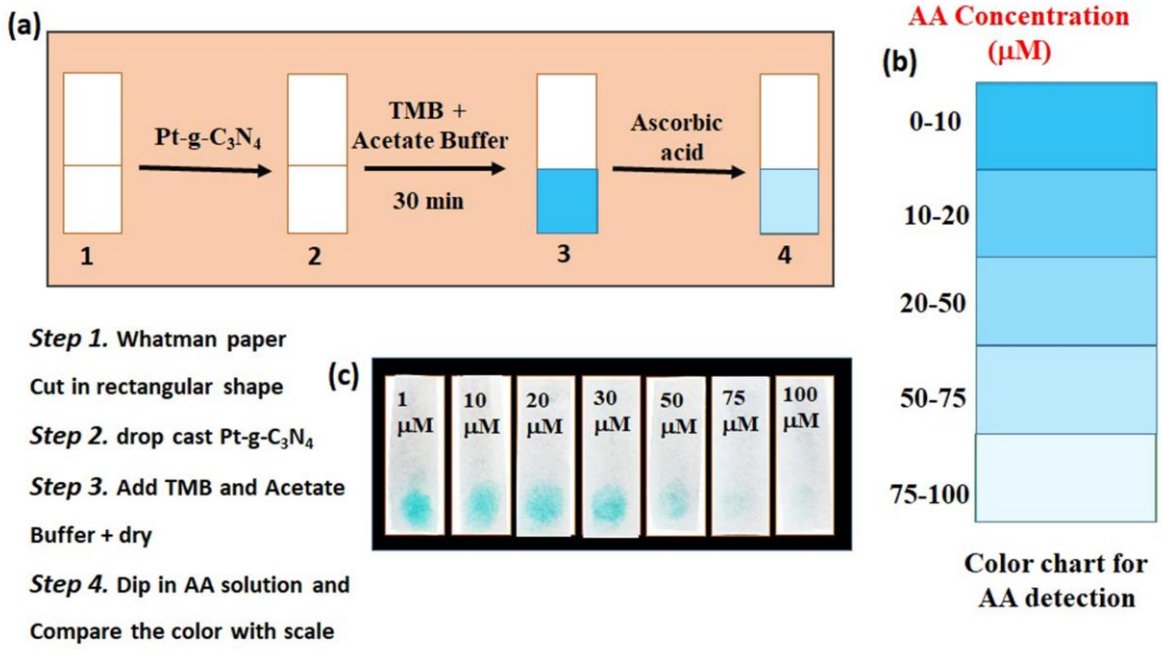


**Figure 5.11** Paper strip kit-based Colorimetry (a) Procedure for using kit (b) Color chart to determine AA conc. (µM) (c) Image showing the color corresponding to different concentrations of AA (Duration for color development = 30 min).

The procedure for fabrication is given in Figure 5.11 (a). In brief, Pt@g-$C_3N_4$ (30 µL) was loaded at one corner of this paper confining in an area of 1 $cm^2$. Further, acetate buffer and TMB were also added and the kit was dried at room temperature in a desiccator. For

studying different concentrations of AA, the kit was dipped in different AA solutions for 30 min. The developed color, as shown in Figure 5.11 (c), was studied using Image-J software, and a standard color chart was developed (Figure 5.11 (b)). To know the concentration of the unknown AA, we have to dip the AA loaded paper in the solution. Finally, the different color contrast was matched with calibrated color chart scale to know the quantitative range of AA in real samples.

**5.4 Conclusion**

In this work, we have fabricated oxidase mimic Pt@g-$C_3N_4$ nanocomposite for colorimetric detection of AA. The Pt@g-$C_3N_4$ nanocomposite has improved mimicking properties due to the excellent coordination of Pt nanoparticles with the surface of nitrogen atoms of g-$C_3N_4$. The simultaneous naked-eye detection of AA has been done. The ascorbic acid sensing is proceeded by taking different concentrations of AA into the mixture of TMB, acetate buffer, and Pt@g-$C_3N_4$. The proposed colorimetric sensing platform is easy to use, highly sensitive, cost-effective, and selective for sensing AA in real samples. Moreover, the synthesized Pt@g-$C_3N_4$ nanocomposite being eco-friendly will benefit human society to use it for AA sensing.